



The technology for detection of gamma-ray burst with GECAM satellite

X. Q. Li¹ · X. Y. Wen¹ · Z. H. An¹ · C. Cai¹ · Z. Chang¹ · G. Chen¹ · C. Chen¹ · Y. Y. Du¹ · M. Gao¹ · R. Gao¹ · K. Gong¹ · D. Y. Guo¹ · J. J. He¹ · D. J. Hou¹ · Y. G. Li¹ · C. Y. Li¹ · G. Li¹ · L. Li¹ · X. F. Li¹ · M. S. Li¹ · X. H. Liang¹ · X. J. Liu¹ · Y. Q. Liu¹ · F. J. Lu¹ · H. Lu¹ · B. Meng¹ · W. X. Peng¹ · F. Shi¹ · X. L. Sun¹ · H. Wang¹ · J. Z. Wang¹ · Y. S. Wang¹ · H. Z. Wang¹ · X. Wen¹ · S. Xiao¹ · S. L. Xiong¹ · Y. B. Xu¹ · Y. P. Xu¹ · S. Yang¹ · J. W. Yang¹ · Q. B. Yi^{1,2} · D. L. Zhang¹ · Fan Zhang¹ · S. N. Zhang¹ · C. Y. Zhang¹ · C. M. Zhang¹ · Fei Zhang¹ · X. Y. Zhao¹ · Y. Zhao^{1,3} · X. Zhou¹ · C. S. Zhang⁴ · J. P. Yu⁵ · L. Chang⁵ · K. K. Zhang⁵ · J. Huang⁵ · Y. M. Chen⁵ · X. B. Han⁵

Received: 15 April 2021 / Revised: 10 September 2021 / Accepted: 29 September 2021 / Published online: 10 November 2021
© Institute of High Energy Physics, Chinese Academy of Sciences 2021

Abstract

Introduction The main physical objective of the GECAM satellite is to detect gamma-ray bursts, which is related to gravitational waves of double compact object mergers. The GECAM satellite also detects and investigates various bursts of high-energy celestial bodies.

Purposes and methods In this study, we designed, developed and calibrated the payload and launched it into orbit with GECAM satellite. The payload consists of the gamma ray detector (GRD, for detecting 4 keV–4 MeV X/γ ray), the charged particle detector (CPD, for detecting 150 keV–5 MeV charged particle), and the electronic box (EBOX). The all-sky field coverage is achieved via two 229-degree large-area satellites positioned 180 degrees apart and are on opposite sides of the geo-center. Each satellite is equipped with 25 GRDs and 8 CPDs; thus, the satellite can identify charged particle bursts in space. Gamma-ray detectors adopt lanthanum bromide crystal technology combined with silicon photomultipliers. This is the first time that this technology was used massively in space detectors.

Conclusions The GECAM satellite can quickly determine the direction of gamma-ray bursts (positioning) via indexing and fitting method, while the transmit variability, energy spectrum and direction of the gamma-ray bursts guide subsequent observations through the Beidou-3 RDSS in quasi-real time. It will play an important role in the study of high energy celestial bursts.

Keywords GECAM · Gamma-ray burst · Lanthanum bromide crystal · Silicon photomultiplier · Beidou short message

X. Y. Wen, X. J. Liu and S. Yang have contributed equally to this work.

✉ X. Q. Li
lixq@ihep.ac.cn

X. Y. Wen
wenxy@ihep.ac.cn

X. J. Liu
liuxj@ihep.ac.cn

S. Yang
yangsheng@ihep.ac.cn

- ¹ Institute of High Energy Physics, CAS, Beijing 100049, China
- ² Xiangtan University, Xiangtan 411105, China
- ³ Beijing Normal University, Beijing 110875, China
- ⁴ Beijing Glass Research Institute, Beijing 101100, China
- ⁵ Innovation Academy for Microsatellites of CAS, Shanghai 201204, China

Introduction

Since its concept was first proposed in 1916, the astronomical observation of gravitational waves has undergone over one century's development and a series of candidate of sources of gravitational wave sources are proposed: precession or merger of double compact star systems (such as neutron stars and black holes), fast-rotating compact objects, supernova outbursts, rotation and merger of supermassive black holes and random gravitational wave background. [1]. In February 2016, the U.S. National Science Foundation announced that, on September 14, 2015, the Laser Interferometer Gravitational-Wave Observatory (LIGO) identified the gravitational wave signals generated by the merger of two black holes [2], signifying the inception of the era of gravitational wave astronomy. Since then, more and more gravitational wave signals have been detected. On August

17, 2017, LIGO, Virgo and other 70 more telescopes worldwide, for the first time, jointly discovered gravitational waves (Numbered GW170817) and gravitational wave gamma-ray bursts (Numbered GRB170817A) generated by the merger of double neutron star. Later, electromagnetic counterparts of optics, soft X-rays and radio waves were discovered [3–9]. The observation of GW170817 was the first time that humans observed the physical process of the same object using gravitational waves and electromagnetic waves, as well as the first- and only-time humans observed gravitational waves and their electromagnetic counterparts, indicating the arrival of the multi-messenger gravitational wave astronomy era.

The merger of double compact stars generates gravitational wave bursts, accompanied by gamma-ray bursts and electromagnetic radiation of other wave bands. As to the combination of various methods for detection of gravitational waves, generated by the merger of double compact stars, and their corresponding electromagnetic signals such as gamma-ray bursts, it is of great significance to find an in-depth understanding of physical laws under extreme conditions such as strong gravitational and strong electromagnetic fields. With current technologies, the positioning of gravitational wave signals is dependent on the time difference of their arrival at different detectors in the ground detector network; the limit of earth scale determines that the limit of spatial positioning capacity of a ground detector network is ~ 10 square degrees. The error of typical positioning provided by ground gravitational wave detectors is several hundred square degrees [3, 10]. The positioning error at this scale extremely limits the subsequent observation by telescopes of other wave bands, making the mission impossible.

According to existing research, the merger of double compact stars generates gravitational waves and radiation of several wave bands such as X/ γ rays, soft X-rays, optics and radio. In these cases, the observation of gamma-ray bursts were the first in terms of time sequence. Therefore, in addition to the research significance of its high-energy radiation in extreme conditions, the detection of gamma-ray bursts also provides a trigger for observation of other wave bands [11, 12]. The positioning accuracy of gamma-ray bursts may reach the scale of degrees or even arcminutes, which is much better than the spatial positioning of the ground gravitational wave detector network, thus enabling feasibility of subsequent observations by providing more accurate location information. Therefore, high-energy detection of gamma-ray bursts is critical for the search of electromagnetic counterparts of gravitational waves.

Since the discovery of gamma-ray bursts in the 1970s, many satellites in the world have carried gamma-ray burst detectors. For instance, the BeppoSAX satellite, which was jointly developed by Italy and Netherlands and launched in 1996, carried five scientific instruments, e.g., LECS, MECS, HPGSPC, PDS and WFC. The PDS was matched

with an NaI(Tl)/CsI(Na) crystal complex for the detection of 20–600 keV X-rays and on-orbit calibration was conducted using an ^{241}Am source. The astronomical satellite Swift Gamma-Ray Burst Mission was jointly developed by the USA, UK and Italy for the observation of gamma-ray bursts; it was launched in 2004 and carried three scientific instruments. The Burst Alert Telescope (BAT) adopted 5200 cm^2 coded aperture imager and operated in the energy range of 15–150 keV [13]. Fermi Gamma-ray Space Telescope (Fermi) was a NASA-led satellite launched with cooperation from USA, France, Germany, Italy and Japan. Launched on June 11, 2008, Fermi carried two detectors: Gamma-ray Burst Monitor (GBM) and Large-Area Telescope (LAT), which operated in the energy ranges 8 keV–40 MeV and 20 MeV–300 GeV, respectively. The GBM consisted of 12 NaI probes and 2 BGO probes, all of which adopted PMT as its photoelectric conversion device. The detection range of NaI probes was 8 keV–1 MeV and that of BGO probes was 200 keV–40 MeV [14]. The hard X-ray monitor (HXM) of Japan's CALET satellite consisted of two lanthanum bromide probes. It adopted a photomultiplier as its photoelectric conversion device with a designed energy range of 7–1000 keV. However, due to humidity absorption of lanthanum bromide, the low energy detection capacity was lost [15].

China's first gamma-ray burst detector was the X-ray detector (SZII/XD) on Shenzhou 2 which was launched in 2001. This detector consisted of two NaI (Tl) probes, both of which adopted PMT as its photoelectric conversion device and operated in the 10–200 keV and 40–800 keV energy ranges, respectively. On-orbit contrast calibration was available in the cross-energy range [16]. Chang'E2 Gamma-Ray Spectrometer (GRS), which was launched on October 1, 2010, adopted lanthanum bromide crystals combined with PMT technology. It only contained one probe, which operated at an energy range of 300 keV–9 MeV [17]. China's first X-ray astronomical satellite Huiyan was launched on June 15, 2017. Huiyan was equipped with 4 detection payloads, i.e., high-energy, medium-energy and low-energy X-ray telescopes and space environment monitors that were able to observe 1–250 keV X-rays and 200 keV–3 MeV gamma-rays. The high-energy X-ray telescope (HE) consisted of 18 NaI(Tl)/CsI(Na) crystal complexes combined with PMT probes. HE provided two detection modes: scanned imaging detection of 20–250 keV X-ray celestial source and detection of 200 keV–3 MeV gamma-ray bursts [18]. China's gamma-ray bursts detectors also include POLAR [19] and GRID [20].

Except for "GRID," which adopted GAGG crystal combined with SiPM, most of the launched gamma-ray detection devices developed at home and abroad basically adopted the technology of combining traditional crystals (e.g., NaI, CsI and BGO) with PMT. The technology of combining traditional crystals with PMT is highly mature after several

decades' development. However, this technology is limited by the light yield of traditional crystals; for example, it's difficult to detect 10 keV energies. Furthermore, PMT requires high-voltage power supply and is influenced by geomagnetic field due to its poor mechanical properties and poor evenness of light collection. Finally, its large size is not favorable for mini designs.

With the arrival of the multi-messenger gravitational wave astronomy era, Chinese scientists proposed the GECAM satellite for detection of gamma-ray bursts which synergizes with gravitational wave events. Named "Huairou 1," the GECAM satellite was the first scientific satellite developed by Space Sciences Laboratory of the Huairou National Comprehensive Science Center (since its establishment). The main scientific objective of the GECAM satellite was to conduct all-time all-sky detection of various burst events, such as gamma-ray bursts related to gravitational wave bursts, magnetar bursts and fast radio bursts. It was able to carry out measurements of energy spectrums and light curves and transmit core information about bursts to ground via satellite-ground real-time communication link, thus guiding subsequent observations [21, 22]. The Institute of High Energy Physics of the Chinese Academy of Sciences took charge of the design and development of payloads of the GECAM satellite. To achieve its objectives, the GECAM payloads should have the capacities listed in Table 1. The main GECAM satellite technical specifications are shown in Table 2.

Hence, we carried out optimized design, development, testing and experimental verification of the GECAM satellite payloads. In this article, we describe the technical achievement of detecting gamma-ray bursts of gravitational waves with payloads. Important tests and experimental verification are introduced, accompanied by the primary results of on-orbit tests of the satellite payloads after launch.

Payload technologies

Design of field-of-view

The payloads of the GECAM satellite include two detectors: gamma-ray radio detector (GRD) and charged particle detector (CPD), which are used for detecting gamma-rays and space charged particles. Furthermore, the payloads were also equipped with an electronics box (EBOX) for signal collection, control, online processing, communication, on-orbit triggered positioning calculation and secondary power distribution of payloads and other functions [21]. The structure of the payloads is shown in Fig. 1. All detectors are evenly arranged on the hemispheric cupola of the satellite dome. The field-of-view of multiple detectors covered all of the sky-all except for the parts covered by the earth. On the round orbit,

with an inclination of 29 degrees and a height of 600 km, two satellites were positioned 180 degrees apart and opposite to the geo-center. Since there are certain overlaps of the field-of-view between the two satellites, all-sky coverage was achieved [21].

Due to the restriction of resources, e.g., weight, size and power consumption of satellites, the GRD adopted a modular compact design. The total detection area of a single GECAM satellite was greater than 800 cm² after division. Then, upon further division, the sensitive area of the GRD monomer was not smaller than 40cm² and there were not less than 20 detectors on a single satellite. In the actual design, the diameter of the GRD crystals was 76 mm [21, 23, 24] with an area of 45.36 cm². The typical background level in space is ~700 count/s/GRD simulated based on the satellite mass model and the AE8/AP8 model in Sect. 2.3. Using this background level and Band soft spectrum [22] as input, we simulated the signal-to-noise ratio (SNR) of the GECAM in the design energy band (8 keV–2 MeV) for various intensity spectra (see Fig. 2). The 3-sigma sensitivity is 2.06e–8 erg/cm²/s (10–1000 keV, 20 s signal duration) for a single satellite.

There were 25 GRD probes on a single satellite, evenly distributed on the surface of a hemispheric cupola. For gamma-ray bursts from any direction not blocked by earth, there were 8–10 probes that were engaged in positioning, thus ensuring adequate positioning accuracy. Furthermore, each satellite was equipped with 8 CPD. The 6 cupolas were distributed in all directions and 2 were located on the side wall of an electronic equipment compartment, to monitor the particle bursts from different directions [21]. Figure 3 shows the effective field-of-view of the payloads. Figure 3 shows that the geometric field-of-view of the payloads not blocked by themselves was 229 degrees. Based on the assumption that the thickness of the atmosphere where gamma-ray bursts would be detected by blocked payloads was 100 km, the field-of-view of the payloads (after being blocked by the earth) was estimated to be 223.6 degrees.

Not all GRDS can detect gamma-ray bursts in any direction; this is largely due to the fact that GRDS are evenly distributed on the surface of the sphere. Figure 4 shows the simulated analysis results of the total receiving area of two satellites detecting gamma-ray bursts in all directions in the sky area; the simulation is based on the current distribution of detectors and the design of the field-of-view of the two satellites, after being arranged on the orbit. The result is calculated via a projection onto the celestial sphere according to the position and direction of each probe in the satellite coordinate system, the satellite orbit and the area of each probe. After 5 days of orbit coverage calculation, the average value is obtained.

Table 1 The scientific requirements and the relevant requirements for payload configuration of GECAM satellite

| Scientific requirements (SR) | Payload configuration |
|--|--|
| SR1: It can monitor the whole day at the same time, and the detection ability of each sky area is basically uniform | The field-of-view of a single satellite should cover all-sky area except the part blocked by the earth Except for the circumstance of shutdown in the abnormal area above South Atlantic, it should operate all-time in rest areas |
| SR2: Its detection sensitivity is higher than that of other mainstream scientific satellites | It should have a large detection area and lower background level, so as to achieve high detection sensitivity ($2E-08$ erg/cm ² /s, 3σ SNR, 10–1000 keV, 700 counts per second background, Band soft spectrum, 20 s signal duration), total detector area > 1500 cm ² |
| SR3: The positioning accuracy of typical brightness gamma bursts (high-energy electromagnetic counterparts) is $\sim 1^\circ$ (1σ , fluence: $10-6$ erg cm ⁻² , time of duration: 10 s) | It should have high positioning capacity, so as to carry out triggering and positioning calculation of gamma-ray bursts on orbit, transmit core information, i.e., positioning information and light variation curve to the ground and timely release it on GCN for guiding subsequent observation There should be at least 5 visible detectors for gamma-ray bursts in each direction that are not blocked by the earth. Otherwise, the location algorithm cannot get sufficient independent detections to obtain an accurate localization |
| SR4: The detection energy range is 10 keV–1 MeV, and it has the ability of energy spectrum measurement | It should cover the many energy range of gamma-ray bursts, in particular, the soft X-ray energy range below 10 keV which cannot be detected by most current gamma-ray detectors on orbit. The detection energy range is 8 keV–2 MeV It should have satisfactory energy resolution and time resolution, so as to carry out high-accuracy detection of gamma-ray bursts |
| SR5: It should be able to distinguish gamma-ray bursts from charged particle events in space | It should be able to identify and exclude space charged particle bursts. The detection energy range of electron is 300 keV–5 MeV |
| SR6: It can trigger, calculate direction and transmit relevant information in real time | It has the functions of on-orbit trigger and positioning and sends the calculation results to the ground in real time |

Energy detection design

Based on the scientific demand of GECAM payloads, the GRD should cover an energy range of 8 keV–2 MeV scintillation crystals with high atomic numbers are adopted for detection of gamma-rays. Although traditional crystals such as CsI(Tl), BGO and PWO satisfy the condition of high atomic number, their light yield cannot satisfy the detection demands since the GECAM should be capable of detecting soft X-rays below 10 keV in addition to gamma-rays. Upon a comprehensive comparison of the property parameters of scintillation crystals, the GRD adopted lanthanum bromide (LaBr₃) crystals [21, 23, 25]. Lanthanum bromide crystals are one of the mass-produced scintillation crystals with the

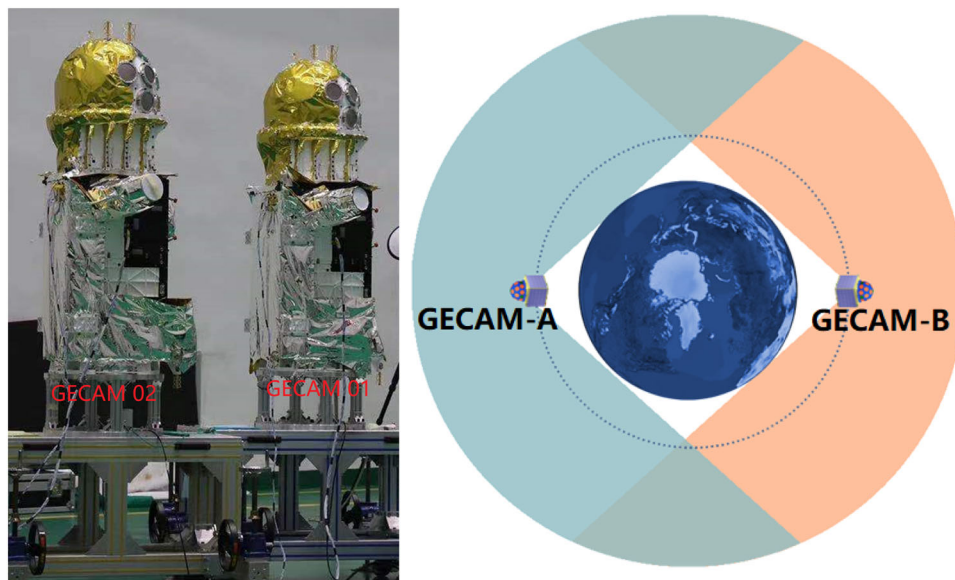
best properties currently available. Their light yield is 63 photons/keV at 662 keV, which is 165% of that of NaI(Tl) crystals; and 47 photons/keV at 5 keV, which is 125% of that of NaI(Tl) crystals. Thus, they demonstrate a satisfactory response to soft X-rays.

To improve the sensitive area as far as possible, in limited electronic channels, the GRD adopted 3-inch diameter lanthanum bromide crystals from Beijing Glass Research Institute. According to the physical simulation results, we finally optimized the thickness of lanthanum bromide crystals to 15 mm (Fig. 5 in ref. [21]). Since lanthanum bromide crystals easily suffer from slaking, they should be sealed. To seal lanthanum bromide crystals, the GRD adopted a 0.2-mm-thick Be sheet as an entrance window. The transmissivity

Table 2 The main technical specifications of GECAM-02 satellite (GECAM-01 satellite is not powered on due to energy problem of solar cells)

| On-orbit test object | Item | Performance index | Remarks |
|----------------------|--|--|---|
| GECAM payload | Sensitivity | $1.11\text{E}-08 \text{ erg/cm}^2/\text{s}$ | SNR: 3 Sigma Background level: ~ 700 counts/s Duration: 20 s Spectrum: Band soft |
| | Positioning accuracy | 2.61° (Single star)/ 0.4° (Double stars, Taking Fermi GBM as equivalent to GECAM-01 satellite) | Fluence: $10^{-6} \text{ erg}\cdot\text{cm}^{-2}$, Duration: 10 s |
| GRD | Number of probes | 25 | One GRD probe |
| | Energy range | 4 keV–4 MeV | |
| | Effective area | 45.3 cm^2 | |
| | Dead time | $4 \mu\text{s}$ | |
| | Energy resolution | $\leq 15.9\%$ @59.5 keV | |
| CPD | Detection efficiency | 78% @8 keV | |
| | Number of probes | 8 | |
| | Energy range (e^-) | 150 keV–5 MeV | |
| EBOX | Gamma-ray detection efficiency | $<7\%$ @8–2000 keV | |
| | Dead time | $4.8 \mu\text{s}$ | |
| | Calculation time of on-orbit trigger and positioning | $<1 \text{ s}$ | |
| | Relative time accuracy of each probe | $0.3 \mu\text{s}$ | |

Fig. 1 Left: Photograph during the GECAM satellite test before launch. Right: Schematic diagram of the blocked field-of-view of the satellites and the overlap of field-of-view of two satellites [21]



of 5 keV X-rays was $>65\%$, which satisfied the requirements for detecting low-energy X-rays. The crystal is packed with an ESR reflector to improve the light collection. The rear end of lanthanum bromide crystals adopted 5-mm-thick quartz glass as a fixing and supporting structure, while serving as a light guide. Lanthanum bromide crystals and quartz glass

were bonded together by optically transparent adhesives. Its internal structure is shown in Fig. 5.

In view of the design demand for the GRD, e.g., miniaturization, low power consumption and strict mechanical conditions, the traditional large-size photomultipliers are no longer appropriate when selecting a photoelectric conver-

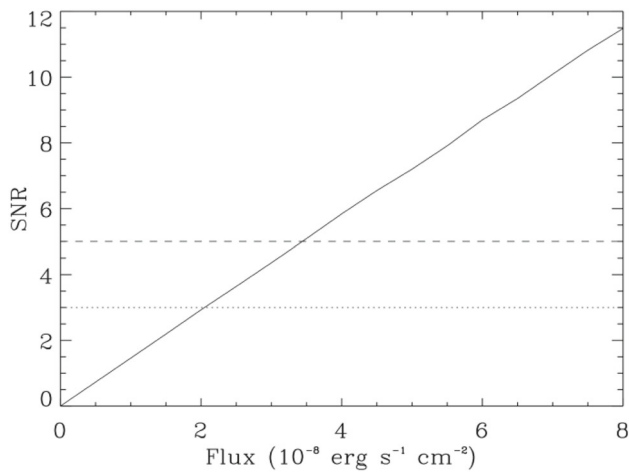


Fig. 2 The relationship between signal-to-noise ratio and energy spectrum intensity. Taking band spectrum as input, the typical GRB energy spectrum is incident, the observation time of the energy spectrum is 20 s

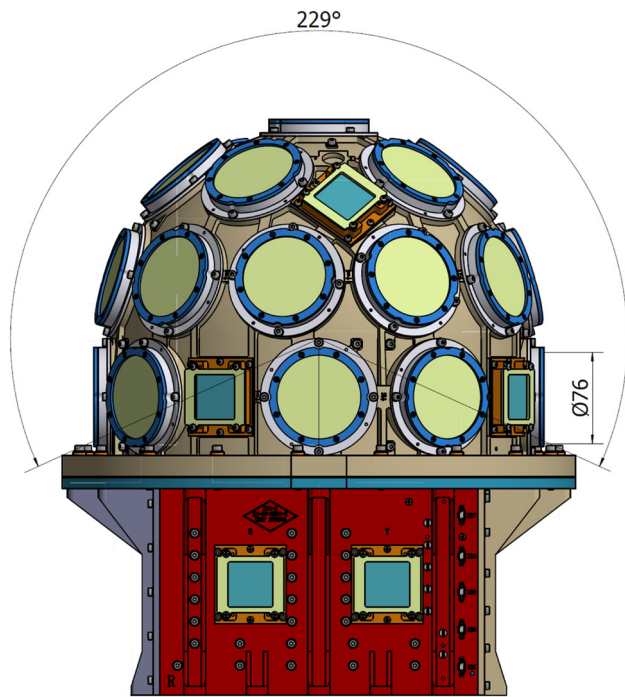


Fig. 3 Effective field-of-view of payloads

sion device; this is largely because of its comprehensive conditions. At the beginning of the design, many small-size multi-anode photomultipliers were also considered. However, they were also not appropriate due to their mechanical properties, weight, size, power consumption and other resources required by a high-voltage power supply. Therefore, we shifted to silicon photoelectric multiplier (SiPM) which has been gradually used in space projects in recent years.

SiPM possesses the typical characteristics of semiconductors. Its merits include its small size, low power consumption

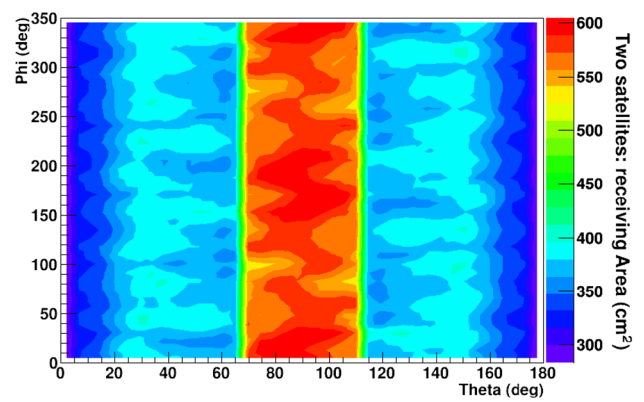


Fig. 4 Simulated analysis result of a sensitive area of the GECAM satellite when detecting gamma-ray bursts. In the figure, theta and phi are the polar and azimuth angles in the payload coordinate system of two satellites in reverse phase operation, respectively

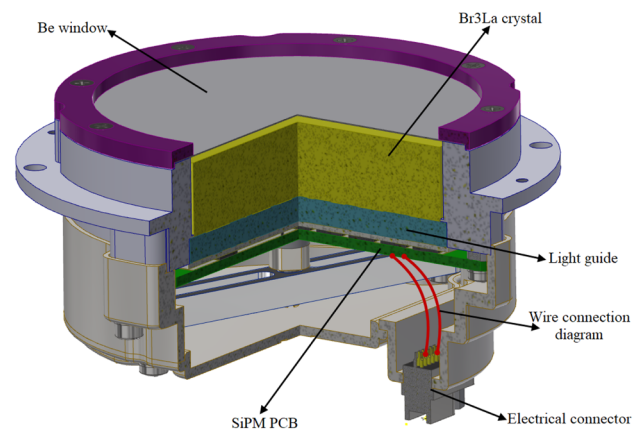


Fig. 5 Illustrated diagram of a GRD structure

and good mechanical adaptability; additionally, it does not require high voltage. Its drawbacks are mainly temperature sensitivity and irradiation damage. Therefore, when selecting semiconductor type and design, all the characteristics of SiPM should be fully considered. In terms of types, the GRD selected MicroFJ-60035-TVS SiPM [19, 21] by SensL Company. The size of each pad is 6.07×6.07 mm and the pixel size is $35 \mu\text{m}$. The fill factor is 76%, and each cell contains 22,292 pixels. The number of pixels per unit area is $605/\text{mm}^2$ and its quantum efficiency curve is 30–40% for 380 nm, which was higher than 20–30% of the traditional PMT. 3200 SiPMs, with a total area of $117,903 \text{ mm}^2$, are used in all the GRDs (64 SiPMs are used per GRD probe).

As shown in Fig. 6, the GRD adopted a parallel readout to combine the SiPM array into one channel of readout and inhibited the thermal noise through the triggering of its threshold value. At the same time, the SiPM was kept smaller noise level at a lower temperature environment through temperature control, thus achieving detection of the low-energy X-rays. Each probe has 64 pieces of SiPM, which are evenly

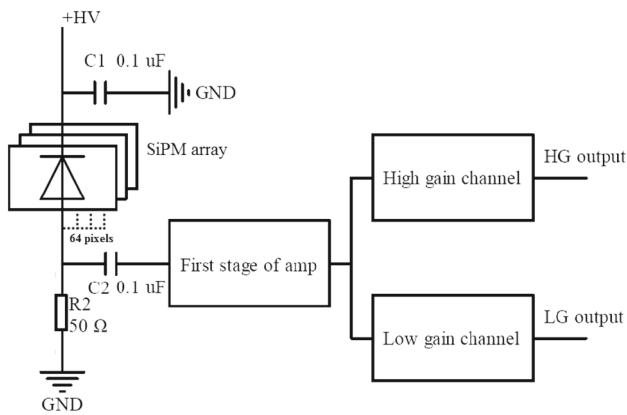


Fig. 6 Circuit diagram of a single GRD

distributed on the circuit board, where the dead space is covered with Tyvek. SiPMs are coupled with the quartz glass through a 1-mm-thick optical rubber pad. To improve the reliability of the detector, each SiPM was provided with two sets of independent power supplies. Normally, both sets of power supplies are applied, which is referred to as a full-component work mode. Once one set of SiPM of a GRD suffers failure, the corresponding GRD will switch to the half-component mode by closing the power supply to the faulty half. Since detectors were on the surface of satellite, the temperature of the SiPM was designed to be within the range of $-17 \sim -23$ °C [26]. An on-orbit temperature compensation circuit was also designed for the GRD. After each SiPM was combined with crystals, the temperature coefficient of each detector was obtained through a calibration test. The actual measurement results suggested that the temperature effect parameter of GRD probes was about $18 \text{ mV}/^\circ\text{C}$ (It contains the contributions of different parts of GRD, which is quite different from the coefficient $21.5 \text{ mV}/^\circ\text{C}$ suggested in the SiPM datasheet). The SiPM temperature was collected via a temperature sensor, then it was converted into digital signals and back fed to the power supply circuit for regulating the bias voltage of the SiPM, thus achieving real-time gain temperature correction and maintaining the stability of SiPM gains.

The required energy measurement range for the GRD was $8 \text{ keV} \sim 2 \text{ MeV}$. The design of the electronic readout covered $4 \text{ keV} \sim 4 \text{ MeV}$. To achieve a greater dynamic range, the front-end electronics of a GRD adopted high- and low-gain readout for processing SiPM signals thus read normal electrical signals at full energy range. The covered energy range with a high-gain readout was $4 \sim 300 \text{ keV}$; the covered energy range with low-gain readout: $40 \text{ keV} \sim 4 \text{ MeV}$.

The calibration device HXCF [27] and a radiation source of the National Institute of Metrology were used for calibration of the E–C relation, energy resolution, detection efficiency, energy response array and detector dead time of GRD

(in the energy ranges of $8 \sim 160 \text{ keV}$ and $200 \text{ keV} \sim 1800 \text{ keV}$, respectively [25]. The detailed result was introduced in the thesis on GRD ground calibration from this collection [28]. Here, the E–C relation of a single detector is given as the representative result, as shown in Fig. 7. It can be learned from Fig. 7 that, 1) in normal temperature, the lower energy threshold value of GRD could reach 8 keV ; 2) The residuals indicate that there is a certain nonlinearity at the absorption edge of high gain and the energy region below 300 keV of low gain. However, this nonlinearity has no significant effect on energy reconstruction. Here, the absorption edge is caused due to Lanthanum K-edge at 38.92 keV and Bromine K-edge at 13.47 keV . The electronic channel ~ 1060 corresponds to 1.8 MeV . Upon extrapolation of an E–C relation, 3500 electronic channels will cover 4 MeV .

Background estimation and time accuracy

Given the relevant physical demand of gamma-ray bursts, the energy range detected by GRD should cover $8 \text{ keV} \sim 2 \text{ MeV}$. The detection efficiency and background level also affect the sensitivity. In addition to the detector's own endogenous background, which affects the background level, the general background of the detector mainly comes from the environmental background of the satellite during on-orbit operation, given that the high particle fluence in the radiation belt and abnormal area above the South Atlantic. In addition, there is a particle sedimentation zone caused by a high-power ground VLF base station in the mid-latitude ($30^\circ \sim 50^\circ$) [29–31]. The satellite adopted a low inclination of 29 degrees to keep the environmental noise at a relatively low level.

As shown in Fig. 8, AP8 and AE8 models were used for estimating the distribution of protons and electron fluence on the 600 km-high circular orbit. The figure shows that the 29-degree orbit inclination avoided the radiation belt, particle sedimentation zone [29–31] and the core of Southern Atlantic Anomaly (SAA). Using GEANT4 simulation software (<http://geant4.cern.ch>) and AE8 / AP8 model, we simulated the background level of GRD. The results show that the average background level of each GRD outside the SAA is about 700 cps.

Both GRD and CPD adopted an event-by-event approach to detect incident X/γ rays and high-energy particles. For each event, the detection time, data collection number, detector number, number of ADC channels and other information were recorded. According to the characteristics of signals, the GRD signals were classified into normal events (the upper energy limit is 4 MeV and the dead time is $4 \mu\text{s}$), super-high events (gamma events exceeding the upper limit of energy of 4 MeV , these kinds of events are recorded in the highest energy channel) and super-wide events (The signal width far exceeds the normal signal, mainly from the contribution of space protons or heavy ion. This is due to the extremely high-

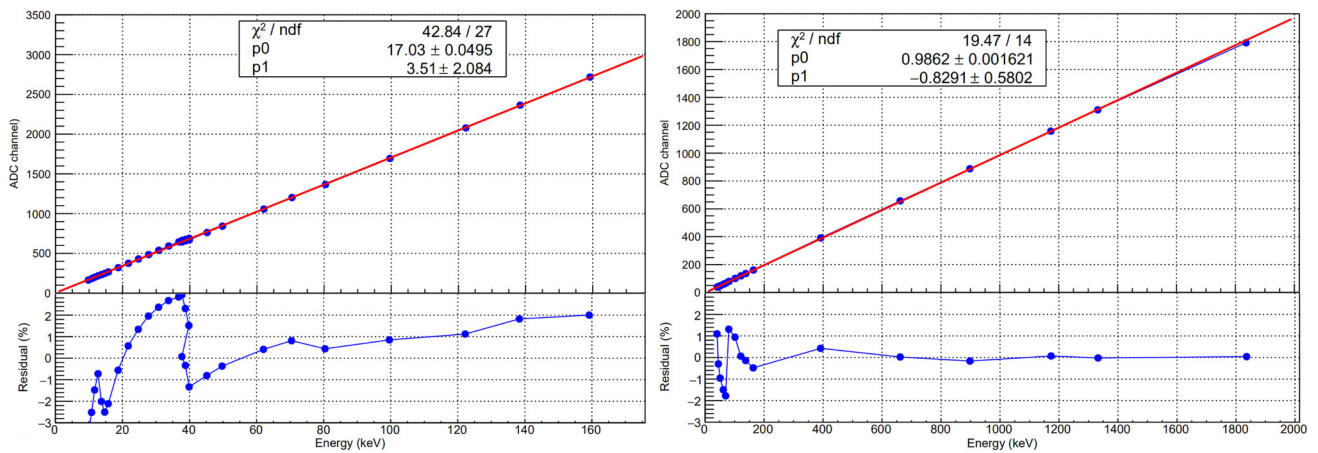


Fig. 7 Representative result of calibration of E–C relation of the GRD. Left: high gain, 8–160 keV, Right: low gain, 37 keV–1.8 MeV. This experiment was performed at room temperature

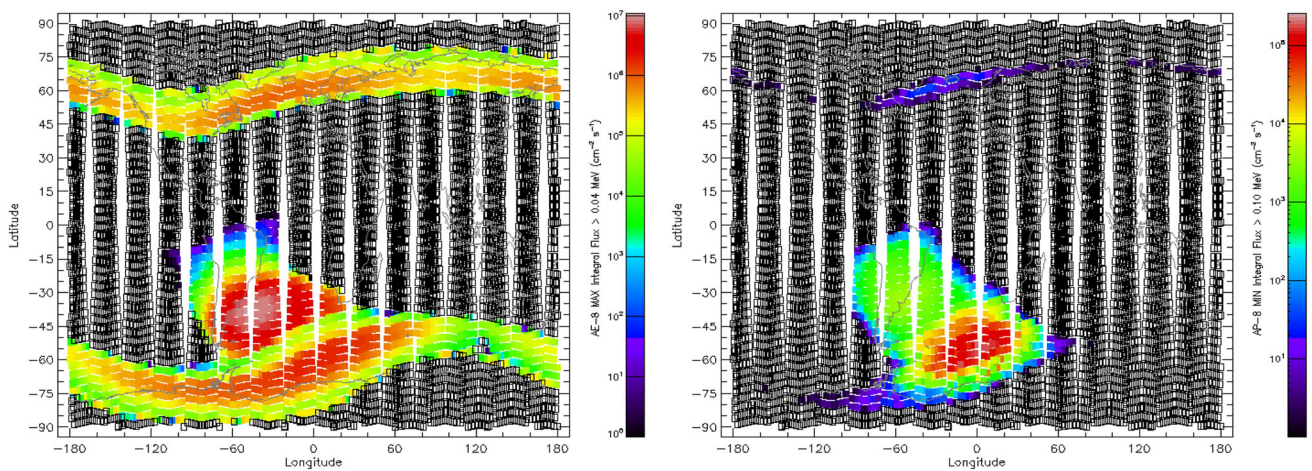


Fig. 8 Distribution of electron (Left) and proton (Right) fluence on the 600 km circular orbit calculated with AP8 and AE8 models (<https://www.spennis.oma.be/>)

energy deposition and the electronics can't response so fast. The dead time of the super-wide event is set at 70 μs . For each event, the dead time was recorded to correct the energy spectrum and flux. The dead time was set to 4 μs for GRD normal events, so that it was not saturated and the effect of pileup can be negligible, even in the event of the brightest gamma-ray burst (For example: GRB 980,329, its fluence is $2.6 \times 10^{-5} \text{ erg/s/cm}^2$ in 50 to 300 keV). It is estimated that the required dead time of GRD is less than 5 μs for this fluence level. For the median flux GRB, the flux level is in the order of $10^{-7} \text{ erg/s/cm}^2$ to $10^{-6} \text{ erg/s/cm}^2$. Given the detection demand, the restraint on the dead time of the CPD was slightly lower than that of GRD and it was designed to be 4.8 microseconds.

In order to detect events such as earth gamma-ray flashes and to exclude space charged particles, the relative time accuracy, that is, the relative deviation of the time recorded by each probe for the same time event (such as the signal from

secondary particles produced by a cosmic ray shower in the satellite of each detector can be approximately regarded as the simultaneous event), of the on-board gamma-ray detector (GRD) and the charged particle detector (CPD) should be less than 0.5 microseconds; this is done to achieve compliance selection and non-compliance identification of all cases. Meanwhile, simultaneous cases were adopted for testing the relative time accuracy of each probe. The GRD and CPD connected to each data acquisition board share the same clock, and the clocks between different circuit boards are compared via GPS broadcast. The actual measured value suggested that the relative time accuracy of on-board probes (including GRD and CPD) was less than 0.3 μs . This will help to distinguish and analyze the terrestrial Gamma-Ray Flash events.

On-orbit triggering and positioning

For detection of gamma-ray bursts, timely provision of accurate burst sources is key to guiding subsequent observation. Therefore, we designed and developed on-board triggering and positioning software. The counting rate of each GRD detector will search the burst source within several time scales and energy ranges. Poisson fluctuation was adopted for calculating the significance of the source. In case the significance exceeds the threshold value, a burst event is recognized and determined as a trigger. In this scenario, the time scale, energy range and significance threshold value were all adjustable parameters. Performance parameters of the payload during on-orbit testing are shown in Table 2.

After gamma-ray bursts were triggered, on-orbit positioning of gamma-ray bursts was conducted with a mesh look-up-table fitting approach [26]. The specific on-orbit positioning algorithm and calculation flows are shown in Fig. 9. We choose the most significant time scale as the best positioning time scale by calculating the significance of the three detectors with the highest significance under four positioning time scales: Trigger time scale, 5 s, 10 s, 20 s. We combine the energy spectrum of the GRD into 8-channels as the input data of the location calculation. The polar angle and azimuth angle of the whole sky are divided into 3072 grids for the positioning template. The rotational angular velocity of the GECAM was $0.06^\circ/\text{second}$ during on-orbit operation. For gamma-ray bursts with longer duration, only the peak part of 10–20 s gamma-ray bursts was adopted for positioning. The peak part concentrated the highest photon number with high signal-to-noise ratio. Therefore, within 10–20 s, the rotation angle of telescope relative to gamma-ray bursts is $< 1^\circ$. According to the direction of the telescope at each second, the rotation of each telescope and the data at different moments were jointly fitted with a positioning algorithm to obtain the positioning. The error was still from the counting error of the detector.

Given the scientific demand of the GECAM satellite, the positioning accuracy for medium-size gamma-ray bursts with typical brightness ($1\text{E-}6 \text{ erg/cm}^2/\text{s}$, 10 s, Band Soft spectrum) should be better than 1° [21] (calculated at the background of 700 cps of a single GRD, with mean value taken at each incidence direction), the adoption of mesh look-up-table fitting approach required that at 5 GRDs, we should be able to receive the signals of gamma-ray bursts from all directions that were not blocked by the earth. During on-orbit operation, the number of response GRDs for gamma bursts is generally between 6 and 12.

After on-orbit triggering, the on-board software of payloads will determine the category of a burst event based on the comparison of counting between the CPD and GRD. If the value exceeds the set threshold (During in orbit test, the event with $\text{CPD}/\text{GRD} > 0.01$ is judged as a charged particle

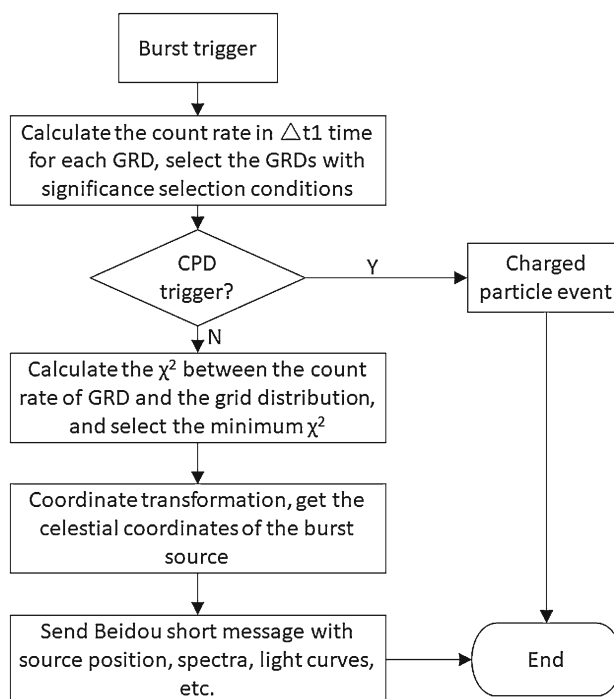


Fig. 9 On-orbit positioning algorithm of GECAM

precipitation event), it is judged as a particle burst. Otherwise, it is considered a gamma-ray burst. If it is judged as a gamma-ray burst, positioning calculation is conducted. The on-board software will conduct positioning of the gamma-ray burst via a mesh look-up-table fitting approach. The calculation time of single trigger is less than 35 ms, and the calculation time of a single positioning takes less than 4 s. Then, the positioning information will be compared with the known source table and the celestial coordinates of known celestial body such as the Sun. At present, this table contains the coordinates of 42 known X-ray celestial sources, such as Vela X-1, crab, Cyg X-1, GRS 1915 + 105, which can be expanded to at most 47.

On-board positioning software can determine whether the bursts come from the occultation of celestial source by earth. If the burst event is not located at the Sun or a known celestial source, an RDSS message is formed (in an agreed format) by considering the energy spectrum, light variation and positioning information of the burst event and transmitted to the ground after being sent to the global RDSS communication link of the Beidou-3 navigation system through the satellite platform; if the burst event is located at the Sun or a known celestial source, it is judged as an occultation event of a celestial source or as a solar flare. The information for the occultation event of a celestial source, solar flare or particle bursts are not downloaded to the ground in the form of an RDSS message. Through verification during the actual on-orbit test, the RDSS message of gamma-ray burst events

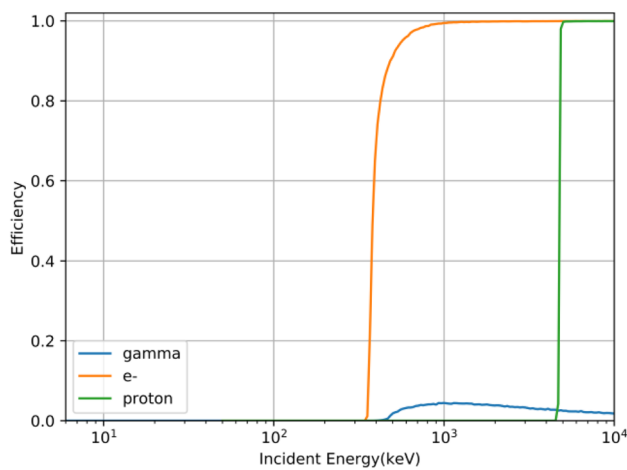


Fig. 10 The efficiency of CPD in detecting gamma-rays and charged particles [21]

triggered on the satellite may be totally downloaded to the GECAM Satellite Science Operation Center in 1 min.

For gamma-ray bursts which can be observed by both satellites, the positioning calculation may be conducted with a time delay algorithm to further reduce the positioning range error. According to the actual measurement result, the relative clock accuracy of the two satellites was small than $1 \mu\text{s}$ (3σ).

Identification of space charged particle bursts

Charged particle bursts occur every day (since the launch, it has been eight times a day on average), which will affect the location and analysis of gamma-ray bursts. Charged particle detectors (CPDs) can monitor changes of the currents of space charged particles in real time, research the background of on-orbit particles and help distinguish GRD-detected gamma-ray bursts and space charged particle events. The CPD adopted a design scheme where plastic scintillators served as sensitive detection materials and silicon photomultiplier (SiPM) served as optic readout devices. According to the requirements on CPD functions, BC-408 plastic scintillators with poor response to gamma-rays and satisfactory optical response to charged particles were adopted. BC-408 plastic scintillators demonstrated a satisfactory light yield and energy linearity against electrons and wave characteristics that were well combined with the SiPM. Upon simulation, optimization, testing and verification, the size of plastic scintillators was designed to be $40 \text{ mm} * 40 \text{ mm} * 10 \text{ mm}$, to achieve high acceptance of space charged particles. As shown in Fig. 10, with the thickness of 10 mm plastic scintillators were much less efficient in detecting X/ γ rays than in detecting charged particles.

CPD adopted the same type of SiPM as adopted in the GRD. Based on the size and structure of the plastic scintil-

lators, each probe of the CPD was provided with 36 SiPMs. To improve the reliability of the detector, each SiPM was provided with two sets of independent power supply. Generally, half of power supply 1 is in operation and the other half (power supply 2) serves as a cold backup. The CPD temperature on the cupola was $-17 \sim -23 \text{ }^\circ\text{C}$, which was the same as that of the GRD. However, the temperature of two CPDs on the side wall of an electronic equipment compartment was higher (within $-30 \sim +20 \text{ }^\circ\text{C}$). Detectors like the GRD and CPD were also designed with an on-orbit temperature correction circuit and the temperature coefficient of all detectors was obtained through a calibration test. The actual measurement results suggested that the temperature effect parameter of the CPD probe was approximately $18 \text{ mV}/^\circ\text{C}$. The SiPM temperature was collected through a temperature sensor, converted into a digital signal and back fed to the power supply circuit for regulating the bias voltage of the SiPM, thus achieving a real-time gain temperature correction and maintaining the stability of SiPM gains.

The flare light of particles after incidence into plastic scintillators was absorbed by the SiPM. Then, the SiPM converted the optical signals into electrical signals. The electrical signals were further amplified by a pre-amplifier and finally connected to a data collection circuit board via cables through an electric coupler. The digitized signals were recorded by a data acquisition electronic system. CPD also provided energy and time information of particles. Based on the ground calibration result, the effective energy range of the CPD in detecting electrons was $150 \text{ keV} \sim 5 \text{ MeV}$, which satisfied the detection index of $300 \text{ keV} \sim 5 \text{ MeV}$.

Figure 10 shows that the efficiency of the GRD and CPD in detecting gamma-rays and charged particles differed greatly. Therefore, through the counting ratio of the GRD and CPD, we can infer whether a burst event consists of gamma-rays or charged particles (mainly the electrons). Based on the ground test result, the identification threshold of particle bursts and gamma-ray bursts was determined. Viewed from the experimental result, the efficiency of CPD in detecting ^{137}Cs (662 keV) gamma is 13.16% of that of GRD in detecting gamma.

Overall consideration of on-orbit calibration

During design of detectors, the on-orbit calibration should also be considered. Since irradiation dose of all crystals will gradually accumulate with the duration of on-orbit operation, their light yield will gradually become poorer, thus causing changes in the E-C relation of the ground calibration. For on-orbit calibration, in addition to the utilization of the spectral line of some celestial sources and background energy spectrum, the characteristic line of crystals and the radioactive source of on-orbit calibration were also considered in the design.

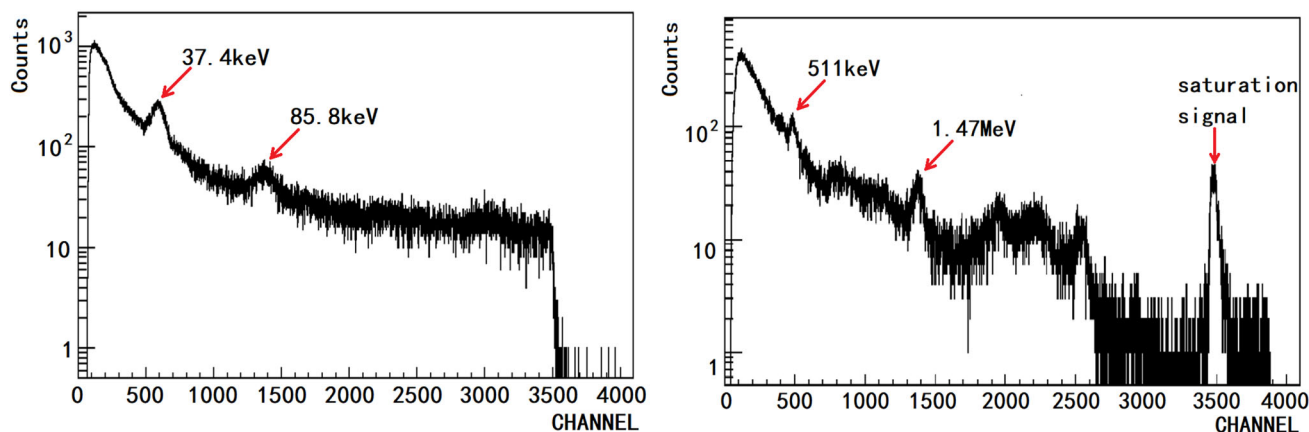


Fig. 11 On-orbit background spectrum of GECAM-02 GRD 1. Left: High-gain energy spectrum, Right: Low-gain energy spectrum

The background energy spectrum detected by on-orbit GRD is shown in Fig. 11. The Lanthanum bromide crystals carry several endogenous spectral lines and those available for on-orbit calibration were mainly the 37.4 keV and 1.47 MeV spectral lines. In addition, there were other lines available for on-orbit calibration, e.g., 59.5 keV characteristic line of CPD imbedded source ^{241}Am , 85.8 keV on-orbit activation spectral line of Bromine in lanthanum bromide crystals and the 511 keV positron electron annihilation line in on-orbit background spectrum. In this way, the on-orbit calibration of the GECAM was basically not dependent on the spectral line of a celestial source to achieve better energy coverage.

For the CPD, since the energy spectrum of space charged particles has no spectral structure, there were no requirements on its energy resolution. However, CPD also used SiPMs and has the characteristics of temperature effect, displacement damage and radiation aging. As to the change of E–C relation caused by these characteristics, rough calibration was conducted via Alpha particle signals of the imbedded source ^{241}Am .

Preliminary results of on-orbit test

At 4:13:37 on December 10, 2020 (Beijing Time), the GECAM satellite was launched into orbit via “two satellites with one rocket” using a Changzheng-11 solid-fueled carrier rocket at Xichang Satellite Launch Center. After entering into orbit, only the GECAM 02 payload is working at present; the payload is in good condition and all functions have been effectively verified. Due to the failure of solar panels, the GECAM 01 satellite payload has not yet started.

Figures 12 and 13 show the energy spectrum of all GRDs and CPDs of the GECAM 02 satellite during on-orbit operation. Figure 12 demonstrates that the spectral shape of

high-gain energy spectrum of all detectors was basically consistent. However, there was a certain difference among low-gain energy spectrum with over 2000 channels, which was related to doping of lanthanum bromide crystals.

Among the installed probes of GRD, there were two kinds of doping of lanthanum bromide crystals: double doping (Cerium 5%, Strontium 1.5%) and single doping (Cerium 5%). For lanthanum bromide crystals with different means of doping, there was a certain difference in terms of nonlinearity at the low energy section. Furthermore, there was also a certain difference in terms of the saturated spectral shape for over 3500 low-gain channels, which was related to the light yield difference of signals of over range event in the two different doped crystals. From Fig. 13, the energy sediment peak of Alpha particles of the ^{241}Am imbedded source on the CPD was seen clearly. The proportion of relative noise was related to the activity of the imbedded source and the size of electronic noise trailing.

By fitting the high gain 37.4 keV peak and low gain 1.47 MeV peak of GRD and the energy sediment peak of alpha particles (5.486 MeV, equivalent electron energy: 570 keV) of the CPD—and through updating of the temperature-bias voltage relation table (18 mV/°C is an average value, and each probe has some differences, which are reflected in the temperature-bias table.) and regulation of bias voltage—the peak position of all probes was adjusted to be consistent with each other. After adjustment, the peak position was consistent, as shown in Fig. 14. In the GRD probe in the left figure, the high gain 37.4 keV peak was obviously divided into two peak positions based on a difference in doping. The consistency of high gain with single doping was: + 1.17%, – 0.93%; whereas, the consistency of high gain with double doping was: + 2.20%, – 3.71% and the consistency of low gain 1.47 MeV peak position was: + 1.71%, – 1.38%. For a CPD probe in the right figure, the consistency of energy sediment peak position of Alpha particles was: + 3.15%, –

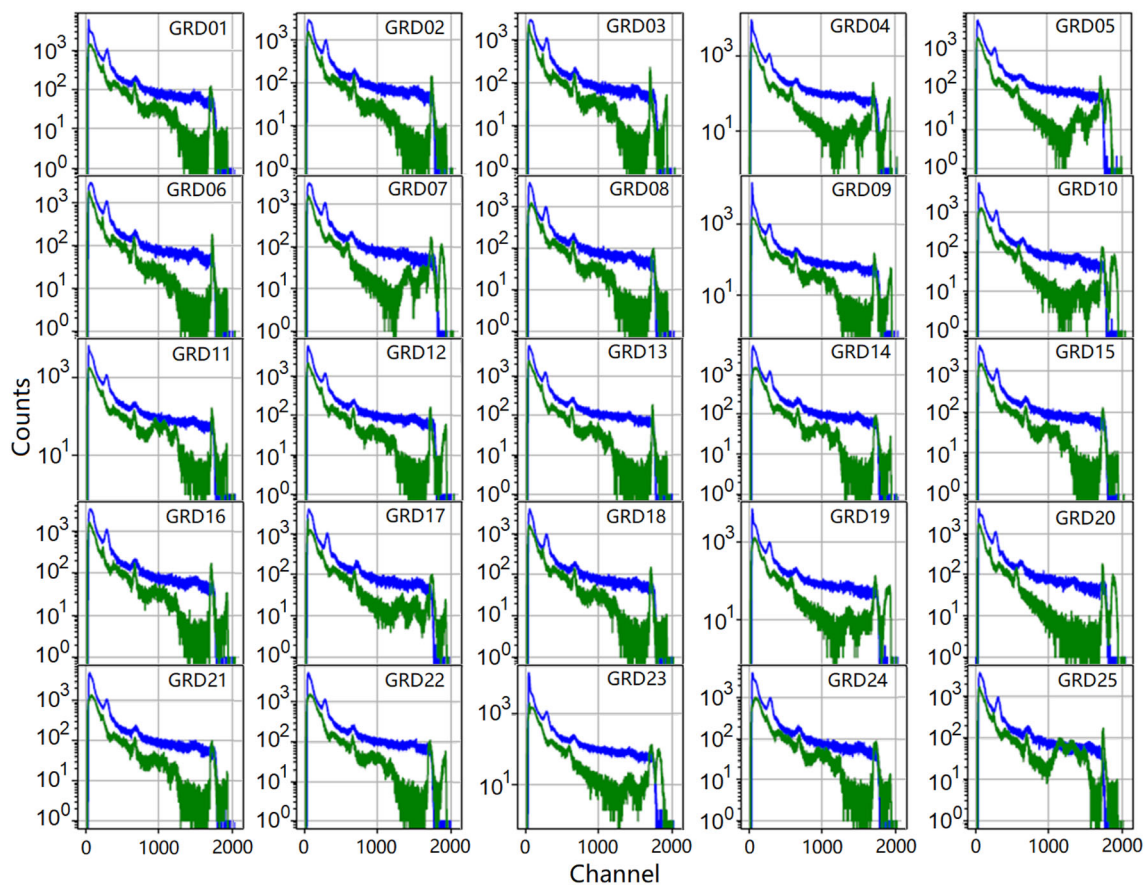


Fig. 12 GRD background energy spectrum of GECAM 02 satellite. The blue curve indicates high-gain energy spectrum, and the green curve indicates low-gain energy spectrum

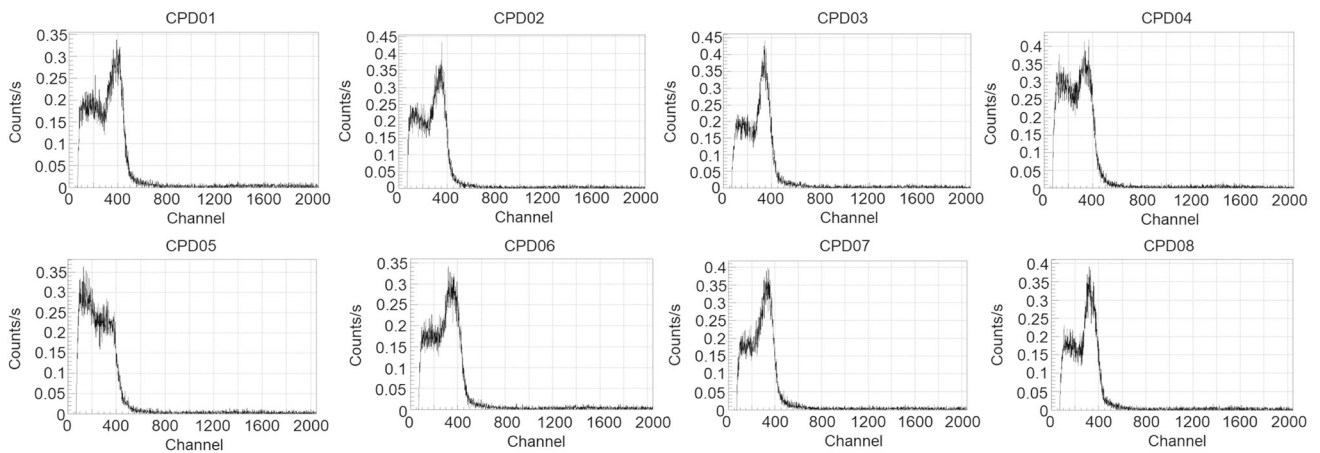


Fig. 13 CPD energy spectrum of GECAM 02 satellite. The peaks near 400 channel of each CPD are from the embedded ^{241}Am source

4.23%. Here, the consistency is the ratio of the maximum deviation points to the mean value. All satisfied the design requirements.

Discussion and summary

The payloads of the GECAM satellite adopted innovative technologies, i.e., a combination of lanthanum bromide crystals with SiPM, on-orbit triggered positioning calculation, global RDSS communication link of Beidou-3 navigation

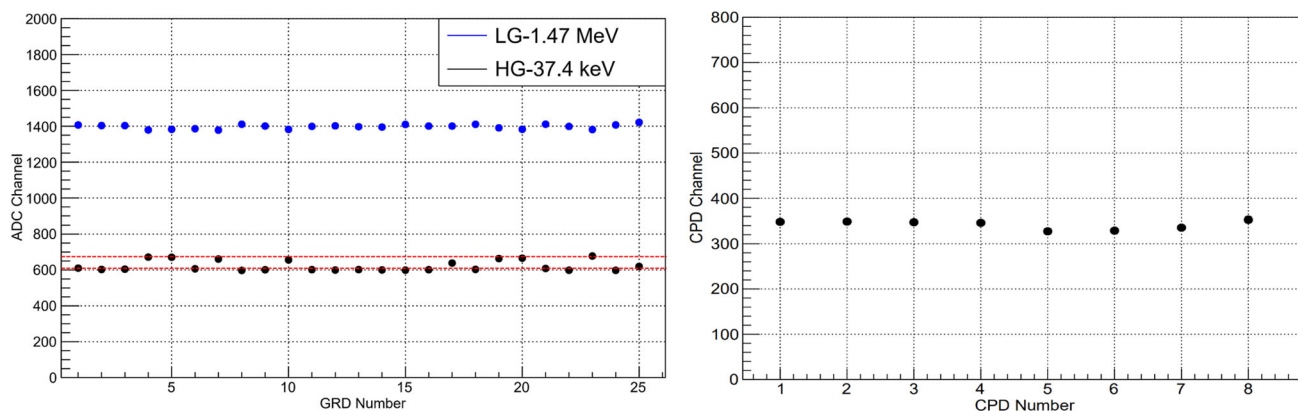


Fig. 14 Consistency of peak position of GRD (left) and CPD (right) of GECAM 02 satellite. In the left figure, the data points on the two upper and lower red lines correspond to the high gain 37.4 keV peak position of the GRD with double-doped and single-doped crystals; the blue data

points refer to low gain 1.47 MeV peak position; the right figure shows the comparison of energy sediment peak position of the alpha particles of all CPD probes

system in systematic design and engineering with combination of orbit environment, carrier parameters and work mode. Detailed tests were performed for the relevant functions and performance during R&D. Furthermore, verification was conducted during on-orbit testing.

Since there is a certain difference between the estimated space radiation environment and the actual circumstance, the displacement damage of the selected type of SiPM is still under assessment. After displacement damage to SiPM is caused by high-energy charged particles, the leakage current will be increased. The impact of this on the payloads of the GECAM includes an increased total probe current and increased noise. After the satellite was launched, with increased duration of on-orbit operation, the trend of increased total probe current and increased noise did exist. However, as of now, the gradient of the increased total probe current is greater than the estimation before the launch. A number of factors, e.g., change of probe temperature, activation effect of crystals and change of counting rate, were involved and caused influences on the total current of probe. In view of the complexity and the demand for application of the technology in the future, analysis and research of such phenomenon are being conducted as special subjects. The related results will be discussed in a future publication.

As to any triggered positioning calculations and the Beidou RDSS download function, they are adequately verified since there are about ten times of triggering every day since on-orbit operation. Regardless of the position of GECAM on the orbit, the triggered alarm information can be transmitted to the ground within 10 min. The application of this function on the GECAM opens a gate for satellites which demand timeliness of information, including astronomical satellites. It can be believed that the global RDSS communication link

of Beidou-3 navigation system will enjoy a wide application prospect.

Acknowledgements The authors wish to thank Professor LIU Zhi-dong, Professor TIAN Zongjun, Researcher WU Jinjie, Professor SHEN Lida, associate Professor QIU Mingbo, senior engineer ZHANG Aimei, associate researcher LI Zhengwei, associate researcher ZHANG Yifei, commander and chief designer of the GECAM Satellite Project and colleagues for their assistance and help in filing and R&D of the project; we thank Beijing Glass Research Institute for producing and supplying sealed lanthanum bromide crystals for GRD detectors; we thank Shandong Aerospace Electronic Technology Research Institute for assistance in engineering, integrated testing and verification of detectors; we thank the National Institute of Metrology for assistance in GRD calibration; we thank the National Space Science Center, CAS for assistance in CPD calibration; and thank Northwest Rare Metal Materials Research Institute for assistance in supplying beryllium pieces. This project is supported by National Natural Science Foundation of China (12173038) and the strategic leading science and technology program (XDA 15360100, XDA 15360102) of the Chinese Academy of Sciences.

References

1. S.L. Shapiro, S.A. Teukolsky, Black holes, white dwarfs, and neutron stars: the physics of compact objects[J]. *Phys. Today* **36**(10), 89–90 (1983)
2. B. Abbott, R. Abbott, T.D. Abbott et al., Observation of gravitational waves from a binary black hole merger[J]. *Phys. Rev. Lett.* **116**(6), 291–311 (2016)
3. B.P. Abbott et al., (LIGO Scientific Collaboration and Virgo Collaboration), GW170817: observation of gravitational waves from a binary neutron star inspiral. *PRL* **119**, 161101 (2017)
4. F. Gbm, A.C. Team, A. Team et al., Multi-messenger observations of a binary neutron star merger[J]. *Astrophys. J.* **848**(2), 1–59 (2017)
5. B. Abbott, R. Abbott, T.D. Abbott et al., Gravitational waves and gamma-rays from a binary neutron star merger: GW170817 and GRB 170817A[J]. *Astrophys. J.* **848**(2), 1–27 (2017)

6. P. D'Avanzo¹, S. Campana¹, O.S. Salafia, et al., The evolution of the X-ray afterglow emission of GW 170817/GRB 170817A in XMM-Newton observations. *Astron. Astrophys.* <http://arxiv.org/abs/1801.06164v2> (2018)
7. A. Murguierberthier, E. Ramirezruiz, C.D. Kilpatrick et al., A neutron star binary merger model for GW170817/GRB 170817A/SSS17a[J]. *Astrophys. J.* **848**(2), L34 (2017)
8. J.J. Ruan, M. Nynka, D. Haggard et al., Brightening x-ray emission from GW170817/GRB 170817A: further evidence for an outflow[J]. *Astrophys. J.* **853**(1), L4 (2018)
9. T. Li, S. Xiong, S. Zhang et al., Insight -HXMT observations of the first binary neutron star merger GW170817[J]. *Sci. China Phys. Mech. Astron.* **61**(3), 1–8 (2018)
10. B. P. Abbott, et al., (LIGO Scientific Collaboration and Virgo Collaboration), GW170814: a three-detector observation of gravitational waves from a binary black hole coalescence. *PRL* **119**, 141101 (2017)
11. LIGO Scientific Collaboration and Virgo Collaboration, Fermi Gamma-ray Burst Monitor, and INTEGRAL, Gravitational Waves and Gamma-Rays from a Binary Neutron Star Merger: GW170817 and GRB 170817A. *Astrophys. J. Lett.* **848**, L13 (2017)
12. C.S. Kochanek, T. Piran, Gravitational waves and gamma -ray bursts. *Astrophys. J.* (1993). <https://doi.org/10.1086/187083>
13. H.A. Krimm et al., The swift/bat hard x-ray transient monitor. *Astrophys. J. Suppl. Ser.* **209**, 14 (2013)
14. C. Meegan et al., The fermi gamma-ray burst monitor. *Astrophys. J.* **702**(791–804), 1 (2009)
15. K. Yamaoka, A. Yoshida, Y. Nonaka, et al., The CALET Gamma-ray Burst Monitor (CGBM). in Proceedings of the 32nd International Cosmic Ray Conference, ICRC 2011 (Vol. 9, pp. 111–114). Institute of High Energy Physics. (2011) <https://doi.org/10.7529/ICRC2011/V09/0839>
16. C.-M. Zhang, Y.-Q. Ma, H.-Y. Wang et al., On border the spaceship “Shen Zhou 2” X ray detector and its calibration and performance at orbit. *Nuclear Electron. Detect. Technol.* **1**, 1–7 (2005)
17. T. Ma, J. Chang, N. Zhang, W. Jian et al., Gamma-ray spectrometer onboard Chang'E-2. *Nuclear Instrum. Methods Phys. Res. Sect. A Accel. Spectr. Detect. Assoc. Equip.* **726**, 113–115 (2013). <https://doi.org/10.1016/j.nima.2013.05.162>
18. S.-N. Zhang et al., Overview to the hard X-ray modulation telescope (insight-HXMT) satellite. *Sci. China Phys. Mech. Astron.* (2020). <https://doi.org/10.1007/s11433-019-1432-6>
19. J. Sun, B. Wu, T. Bao, et al., Performance study of the gamma-ray bursts polarimeter POLAR[J]. in Proceedings of SPIE (2016)
20. J. Wen, X. Long, X. Zheng, Y. An, H. Feng, M. Zeng et al., GRID: a student project to monitor the transient gamma-ray sky in the multi-messenger astronomy era. *Exp. Astron.* **48**, 77 (2019)
21. X. Li et al., The GECAM and its payload. *Sci. Sin. Phys. Mech. Astron.* **50**(12), 129508 (2020). <https://doi.org/10.1360/SSPMA-2019-0417>
22. Band et al., BATSE observations of gamma-ray burst spectra. I. Spectral diversity. *ApJ* **413**, 281 (1993)
23. D. Zhang, X. Li, S. Xiong et al., Energy response of GECAM gamma-ray detector based on LaBr 3: Ce and SiPM array. *NIMA* **921**, 8–13 (2019)
24. D. Guo, W. Peng, Y. Zhu, G. Li, J. Liao, S. Xiong, R. Qiao, X. Li, Z. An, Y. Xu, S. Yang, D. Zhang, X. Sun, Energy response and in-flight background simulation for GECAM. *Sci. Sin. Phys. Mech. Astron.* **50**(12), 129509 (2020). <https://doi.org/10.1360/SSPMA-2020-0015>
25. R.-Q. Song, Z.-H. An, J.-J. Wu, W.-C. Lai, S.-M. Guo, P.-Y. Zhou, X.-Q. Li, Research on the performance of GECAM satellite LaBr 3(Ce)detector in low energy region. *Nuclear Electron. Detect. Technol.* **3**, 467–473 (2020)
26. V. Connaughton et al., Localization of gamma-ray bursts using the fermi gamma-ray burst monitor. *ApJS* **216**, 32 (2015). <https://doi.org/10.1088/0067-0049/216/2/32>
27. X. Zhou, X. Li et al., Introduction to a calibration facility for hard X-ray detectors. *Exp. Astron.* **38**(3), 433–441 (2014)
28. Z. An, et al., The design and performance of GRD onboard the GECAM satellite, RDTM, GECAM special issue, 2021 (the detail need to be updated)
29. Z. Zhang, L. Chen, X. Li et al., Observed propagation route of VLF transmitter signals in the magnetosphere. *J. Geophys. Res. Space Phys.* **123**(7), 5528–5537 (2018). <https://doi.org/10.1029/2018JA025637>
30. Z.X. Zhang, X.Q. Li et al., North west cape-induced electron precipitation and theoretical simulation. *Chin. Phys. B* **25**(11), 119401 (2016)
31. X. Li et al., Study of the North West Cape electron belts observed by DEMETER satellite. *J. Geophys. Res. Space Phys.* **117**, A04201 (2012)